J. Marine Sci. Appl. (2016) 15: 16-27
DOI: 10.1007/s11804-016-1337-y

Simulation of Hydrodynamic Performance of Drag and Double Reverse Propeller Podded Propulsors

Chunyu Guo*, Pengfei Dou, Tao Jing and Dagang Zhao

School of Shipbuilding Engineering, Harbin Engineering University, Harbin 150001, China

Abstract: The unsteady performance of drag and double reverse propeller podded propulsors in open water was numerically simulated using a computational fluid dynamics (CFD) method. A moving mesh method was used to more realistically simulate propulsor working conditions, and the thrust, torque, and lateral force coefficients of both propulsors were compared and analyzed. Forces acting on different parts of the propulsors along with the flow field distribution of steady and unsteady results at different advance coefficients were compared. Moreover, the change of the lateral force and the difference between the abovementioned two methods were mainly analyzed. It was shown that the thrust and torque results of both methods were similar, with the lateral force results having the highest deviation

Keywords: podded propulsor, propeller, lateral force, computational fluid dynamics (CFD), hydrodynamic performance, moving mesh method

Article ID: 1671-9433(2016)01-0016-12

1 Introduction

In recent years, podded propulsors have been introduced as a new type of electric ship propulsion system. Owing to the superior performance of this system, an increasing amount of research has occurred in this field. Institutions such as the Hamburgische Schiffbau-Versuchsanstalt and the Maritime Research Institute Netherlands have developed detailed test methods for determining the hydrodynamic performance and self-propulsion factors (The Propulsion Committee, 2002) of podded propulsors and have proposed test procedures for the propulsors in open water (Mewis, 2001). Ohashi and Hino (2003) used a computational fluid dynamics method to simulate and study interactions between podded propulsors and ships' hulls. Liu *et al*. (2009) numerically simulated unsteady moment, torque, and thrust of Drag Podded Propulsor (DPP) models under various steering angles and found that the hydrodynamic load strongly affects the blade, pod, and strut of the propulsors. Thus, they concluded that the hydrodynamic load is a factor that cannot be ignored when assessing propulsor fatigue strength and maneuverability. Bal and Güner (2009) combined the boundary element and vortex lattice methods to simulate propeller-pod interaction, and force distribution on the pod and strut. They noted that the strut causes the velocity of water to increase at the pod surface (especially in areas near the strut) and that the pod causes the velocity to increase at the strut surface (especially in areas near the pod). They validated the feasibility of their proposed method through comparisons with experiments. Using preliminary Reynolds-averaged Navier-Stokes (RANS) analysis, Shamsi and Ghassemi (2014) compared the thrust and lateral forces on drag- and push-type propulsors, producing calculation results that agreed well with test results.

In China, Yang *et al*. (2003) investigated the impact of a podded propulsor on the hydrodynamic performance of a propeller using theoretical computation and experimental methods to study the steady hydrodynamic performance of single-propeller podded propulsors. Using systematic computation and an analysis of the unsteady hydrodynamic performance of a propeller in the presence of a pod, Ma (2006) conducted a detailed study of the individual impacts of propeller load and pod and strut wakes as well as the impacts of nominal and effective wakes on POD propulsors. Cao *et al*. (2003) used the Cavitation Tunnel Laboratory at Shanghai Jiaotong University to conduct experiments on various podded propulsor models. Their results showed that the presence of any type of podded propulsor, including double propellers in tandem and single drag or push propellers, led to improved open water efficiency compared to conventional propeller systems. However, the efficiency of the overall podded propulsor system of their study decreased when the resistance caused by the pod was considered.

Guo *et al*. (2009a) used a FLUENT RANS solver to compute the hydrodynamic performance of a DPP under uniform and oblique flow states. Mixed-surface model and moving mesh method were used to study the steady and unsteady performances of the blade, strut, and pod of the model; they also presented a preliminary discussion of the lateral force on the strut and pod when sailing straight or at various oblique flow angles. Zhuang *et al*. (2013) investigated the mutual interference between the front and

Received date: 2015-05-22
Accepted date: 2015-10-14
Foundation item: Supported by National Natural Science Foundation of China (41176074, 51209048,51379043,51409063); High tech ship research project of Ministry of industry and technology (G014613002); The support plan for youth backbone teachers of Harbin Engineering University (HEUCFQ1408)
***Corresponding author Email:** guochunyu@hrbeu.edu.cn

rear propellers of a podded propulsor by combining *multiple reference frame (MRF)* and moving mesh models. They proposed that the stream of a double-propeller podded propulsor is unsteady when performing numerical computations for the rear propeller owing to the effects of the front propeller. Hence, it is reasonable to use a moving mesh model for simulations.

The present study is based on the findings of the abovementioned previous studies. The steady and unsteady methods were combined with the moving mesh model to study and compare the hydrodynamic properties of drag and Double Reverse Propeller Podded Propulsors (DRPPPs).

2 Numerical Computation Methods

2.1 Governing equation

We used the RANS equation as the controlling formula for our computation. Assuming that a fluid within the flow field is incompressible, the following continuity and momentum equations were obtained (Guo *et al*., 2010a):

$$\rho\frac{\partial u_i}{\partial x_i}=0 \tag{1}$$

$$\rho\frac{\partial(u_iu_j)}{\partial x_j}=-\frac{\partial p}{\partial x_i}+\rho\frac{\partial}{\partial x_j}\left[\nu\left(\frac{\partial u_i}{\partial x_j}+\frac{\partial u_j}{\partial x_i}\right)\right]-\frac{\partial}{\partial x_j}(-\rho\overline{u_i'u_j'}) \tag{2}$$

where u_i and u_j represent time-averaged velocity components (i, j = 1, 2, 3); x_i and x_j represent the components of the coordinate system in the horizontal and vertical directions, respectively; p is the time-averaged pressure; ρ is the fluid density; ν is the fluid kinematic viscosity coefficient; g is the acceleration due to gravity; and $-\rho\overline{u_i'u_j'}$ is the Reynolds stress term.

2.2 Turbulence model

The *RNG k-ε* was used as a turbulence model because it is more suitable for modeling the effects of rotating machinery. In *RNG k-ε*, a series of successive transformations at any random spatial scale is used to achieve a coarse-resolution description of a system or process that is originally very complex, allowing small-scale motion systems to be eliminated from the control equation (Guo *et al*., 2009b) as follows:

$$\mathrm{d}\left(\frac{\rho^2k}{\sqrt{\varepsilon\mu}}\right)=1.72\frac{\mu_{\mathrm{eff}}/\mu}{\sqrt{\left(\frac{\mu_{\mathrm{eff}}}{\mu}\right)-1+C_\nu}}\mathrm{d}\left(\frac{\mu_{\mathrm{eff}}}{\mu}\right) \tag{3}$$

where k and ε satisfy

$$\rho\frac{Dk}{Dt}=\frac{\partial}{\partial x_j}\left[\alpha_k\mu_{\mathrm{eff}}\frac{\partial k}{\partial x_j}\right]+P-\rho\varepsilon \tag{4}$$

$$\rho\frac{D\varepsilon}{Dt}=\frac{\partial}{\partial x_j}\left[\alpha_\varepsilon\mu_{\mathrm{eff}}\frac{\partial\varepsilon}{\partial x_j}\right]+C_{1\varepsilon}\frac{\varepsilon}{k}P-C_{2\varepsilon}\rho\frac{\varepsilon^2}{k} \tag{5}$$

Here, k is the turbulent kinetic energy, ε is the dissipation rate of the turbulent kinetic energy, t is time, ρ is the fluid density, x_j is the component of the coordinate system in the vertical direction, μ_{eff} and μ are turbulent viscosity terms, $C_\nu\approx100$ is a constant, and P is the output of the turbulent kinetic energy; $\alpha_k=1.0$, $\alpha_\varepsilon=1.3$, $C_{1\varepsilon}=1.44$, and $C_{2\varepsilon}=1.92$.

2.3 Selection of computation method

A combination of the MRF and moving mesh models was used as the computational model in this study. The MRF model was used to implement the steady method; for the unsteady method, the MRF model was used to provide the initial flow field, and the moving mesh model was used to complete the entire computation.

The moving mesh model allows meshes on both sides of an interface to slide over each other without an overlap of mesh nodes on either side. For this purpose, the flux across both sides must be computed and made equal. When computing the flux, first, for each time step, it is necessary to determine overlapping surfaces on both sides of the interface; essentially, the flux through the overlapping surfaces of the mesh is computed based only on overlapping surfaces within boundary domains on both sides of the interface, rather than the entire interface.

For computations under the unsteady flow, the interface where meshes mutually slide is formed by the area within the fluid machinery between the rotating component's outlet and stationary component's inlet (Fig. 1). A moving mesh model must be used to compute the unsteady flow field when a real-time (instead of time-averaged) solution is applied to interactions between the rotor and stator (Wang *et al*., 2011).

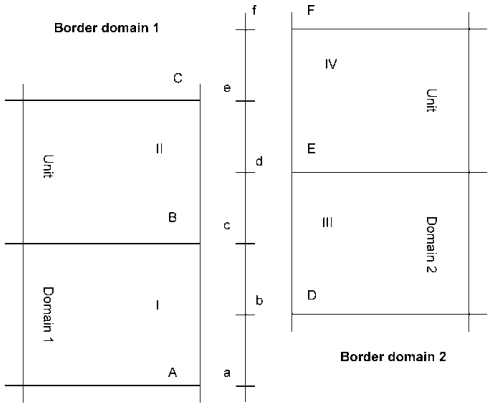

Fig. 1 Sketch of data transmission between static and moving meshes

3 Establishing the Computation Model

3.1 Building the geometric model

The geometric parameters (Li *et al*., 2009) for the propeller of the podded propulsor model used for computation are shown in Table 1; those for the pod, strut, and other components are shown in Table 2 and Fig. 2. The

pod and propeller hub, both of which are parts of a podded propulsor, are merged to form an ellipsoidal rotator. The cross-section of strut is oval.

Table 1 Geometric parameters of propeller

Parameter	Measurement
Number of blades	4
Diameter / m	0.24
Side bevel / (°)	35
Pitch ratio / (0.7 *R*)	1.284

Table 2 Other parameters of podded propulsor

Parameter	Measurement / m
Major axis of cross-section of strut	0.18
Minor axis of cross-section of strut	0.036
Height of strut surface along Y axis	0.19
Distance between centers of the two propeller disks of a double-propeller podded propulsor	0.31
Combined length of pod and propeller hub	0.4
Length of propeller hub	0.075 2
Maximum pod diameter (m)	0.1

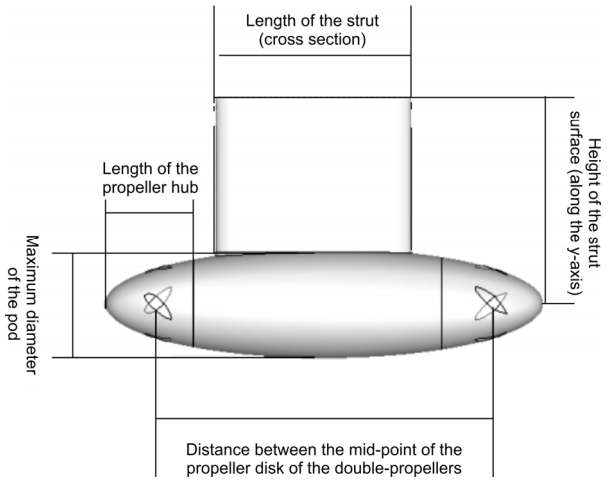

Fig. 2 Geometric parameters of pod and strut

The computation model was constructed using the *O-XYZ* Cartesian coordinate system; for the propeller, the coordinates of the origin (0, 0, 0) were fixed at the center of the propeller disk. For a DRPPP, the coordinates for the centers of the front and rear propeller disks were fixed at (0, 0, 0) and (0.31, 0, 0), respectively. In the positive direction of the *X* axis, the axis of rotation along the propeller pointed downstream. In the positive direction of the *Y* axis, the bus bar along the strut of the podded propulsor pointed toward the pod exterior. The *Z* axis complied with the right-hand rule. The specific model is shown in Fig. 3, where (a) and (b) represent the DPP and DRPPP, respectively.

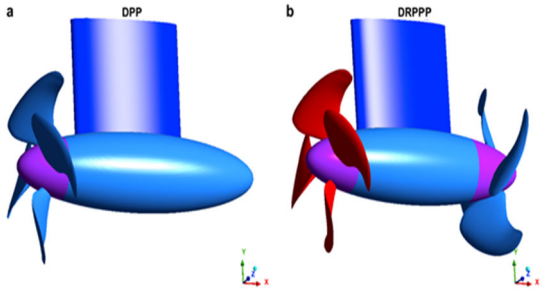

Fig. 3 Podded propulsors and coordinate system

3.2 Partitioning the mesh

The mesh quality is a critical factor affecting the accuracy of numerical simulations; specifically, a high-quality mesh can effectively enhance the accuracy of simulation results. The mesh quality is in turn determined by the form and the mesh number. Because the viscous force has different degrees of impact on the thrust and torque of the propeller blade, the torque coefficient of the podded propulsor is especially sensitive to the mesh quality (Zhang, 2008).

For this study, the propeller and its hub were placed within Domain 1, a cylindrical control domain with a diameter slightly larger than that of the propeller, after which the mesh within the domain was refined. Domain 2 was the control domain for the pod and strut, and Domain 3 represented the flow field. The specific partitioning of the computational domains is shown in Fig. 4. During computation, two types of meshes—unstructured and structured—were used. As the large surface curvature and complex structure of the podded propulsor in Domains 1 and 2 made the use of a structured mesh unsuitable, an unstructured mesh was used for the internal areas of these two domains.

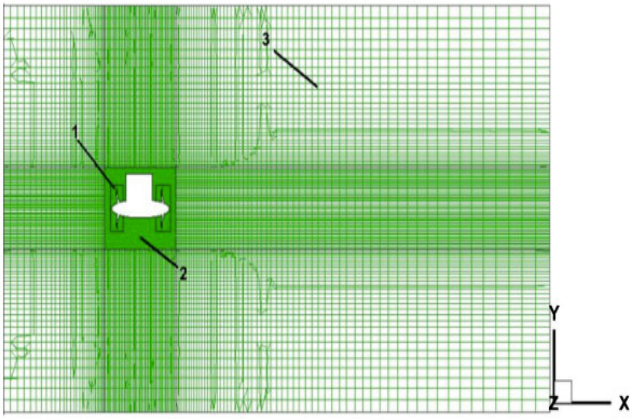

Fig. 4 Mesh of calculation model

4 Analysis of results of numerical computations

4.1 Comparison of computational and experimental values for podded propulsors

For the computations, the propeller speed was set at n=1 200 r/min. the stream velocity V_A was adjusted so that the advance coefficient J took the discrete values 0.5, 0.6,

0.7, 0.8, and 0.9.

The relationships among the advance coefficient J, the thrust coefficient K_T, the torque coefficient K_Q, and the open water efficiency η are as follows: advance coefficient $J=\frac{V_A}{nd}$; thrust coefficient $K_T=\frac{T}{\rho n^2 d^4}$; torque coefficient $K_Q=\frac{Q}{\rho n^2 d^5}$; open water efficiency (single-propeller) $\eta=\frac{K_T}{K_Q}\cdot\frac{J}{2\pi}$; and open water efficiency (double-propeller) $\eta_0=\frac{J}{2\pi}\cdot\frac{K_{T_F}+K_{T_A}}{K_{Q_F}+\frac{n_A}{n_F}K_{Q_A}}$, where ρ is the fluid density, T is the thrust, Q is the torque, n is the rotational speed, d is the outer diameter of the propeller, K_{T_F} and K_{T_A} are the respective thrust coefficients of the front and rear propellers, K_{Q_F} and K_{Q_A} are the respective torque coefficients of the front and rear propellers, and n_F and n_A are the respective rotational speeds of the front and rear propellers.

The thrust and torque coefficients of the two types of podded propulsors under various advance coefficients were computed using FLUENT simulations. For the steady method, the computed values were adopted directly; for the unsteady method, the time-average values of the computed data were used instead. The computed results and experimental values (Guo *et al*., 2010b) were then compared and are shown in Tables 3 and 4.

Table 3 DPP: Comparison of computational and experimental values for thrust and torque coefficients

J	Experiment		Steady method				Unsteady method (time-average)			
	K_{TB}	$10K_{QB}$	K_{TB}	Error / %	$10K_{QB}$	Error / %	K_{TB}	Error / %	$10K_{QB}$	Error / %
0.5	0.363	0.572	0.354 1	−2.50	0.596 5	+4.10	0.354 2	−2.48	0.595 9	+4.01
0.6	0.32	0.52	0.313 5	−2.08	0.544 3	+4.46	0.313 8	−1.98	0.544 0	+4.41
0.7	0.273	0.464	0.270 0	−1.10	0.487 2	+4.77	0.270 3	−0.99	0.486 8	+4.68
0.8	0.228	0.409	0.223 6	−1.95	0.424 7	+3.70	0.224 0	−1.79	0.423 4	3.41
0.9	0.181	0.345	0.175 0	−3.43	0.354 8	+2.77	0.175 2	−3.31	0.353 0	2.27

Table 4 DRPPP: Comparison of computational values for thrust and torque coefficients

J	Steady method		Unsteady method (time-average)		Error /%	
	K_{TB}	$10K_{QB}$	K_{TB}	$10K_{QB}$	K_{TB}	$10K_{QB}$
0.5	0.634 1	1.167 9	0.645 5	1.189 1	1.77	1.78
0.6	0.561 8	1.071 8	0.572 0	1.089 7	1.78	1.64
0.7	0.483 6	0.963 8	0.493 0	0.981 0	1.90	1.75
0.8	0.401 2	0.845 1	0.406 0	0.855 1	1.19	1.17
0.9	0.316 5	0.717 0	0.321 7	0.727 8	1.63	1.49

Table 3 shows that, for the DPP, a certain amount of deviation exists between the Fluent simulations and the experimental values for the K_T and $10K_Q$ values. However, within the computational range of the advance coefficients, the match between the two sets of values is good; the computational and experimental values are essentially consistent and differed within a 5% error margin. This result deminstrates that the proposed method is reliable for forecasting the hydrodynamic performance of a DPP. A comparison of the numerical and experimental results for the thrust and torque coefficients of the DRPPP is shown in Table 4. Again, rhe results of the two methods are very close and within a 2% error margin.

It is seen that, for the DPP, the time-average values derived using the unsteady method are more accurate than those using the steady method. This illustrates that the assumptions of the unsteady method are more reasonable and closer to reality.

4.2 Force analysis of both types of podded propulsors

4.2.1 Analysis of thrust and torque coefficients of propulsors using steady method

The total thrust coefficient curves of the two types of podded propulsors are shown in Fig. 5. Figs. 6 and 7 show the thrust and torque coefficient curves, respectively, for several types of propellors. For the DRPPP, the total torque coefficient (Fig. 7), is the sum of the absolute values for the front and rear propellers (in the figures, DRPPP-front stands for front DRPPP propeller and DRPPP-rear stands for DRPPP rear propeller). The following observations can be made from Figs. 5–7:

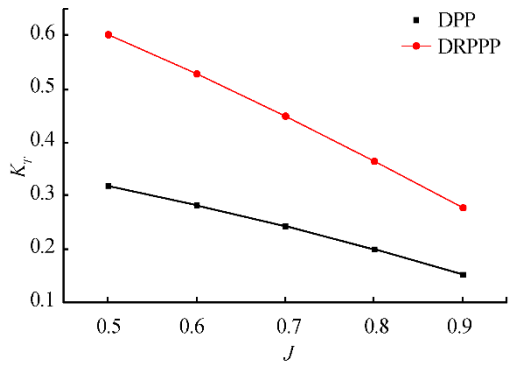

Fig 5 Thrust coefficient curves of podded propulsors

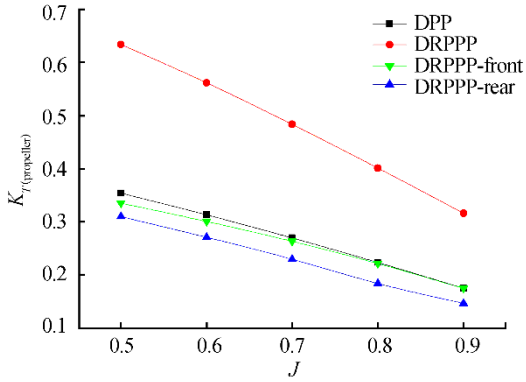

Fig 6 Thrust coefficient curves of propellers

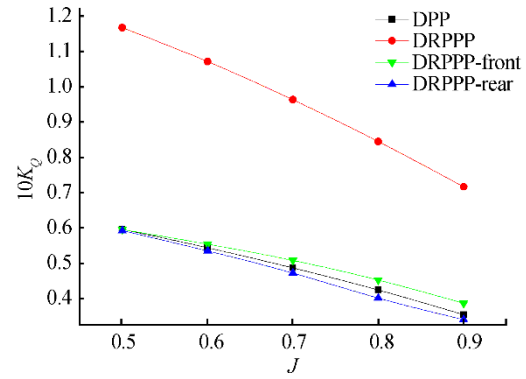

Fig 7 Torque coefficient curves of propellers

1) The thrust and torque coefficients for both the propulsors and the propellers decreases linearly with as the advance coefficient increases.

2) From Figs. 5 and 6 it is seen that the resistance of the pod and strut reduces the total thrust of both podded propulsors below that of the propellers.

3) The thrust and torque coefficients of the DRPPP are significantly larger than those of the DPP, but the DRPPP curves shows the largest rate of decrease with increasing advance coefficient. In addition, the DRPPP propellor thrust is always lower than that of the DPP propellor (Fig. 6).

4) The torque coefficients of the DRPPP propeller are about twice of that of the DPP; furthermore, the torque of the front propeller is higher than the torque of the DPP' propeller but the torque of the rear propeller is lower than that of DPP.

4.2.2 Analysis of thrust and torque coefficients of propulsors using unsteady method

The unsteady results are similar to sine curves and vary by advance coefficient; here, $J = 0.7$ is used as an example for analysis. The thrust coefficient of the propeller blade, overall thrust coefficient, and torque coefficient of the DPP and DRPPP are shown in Figs. 8-10, respectively. The computational curves of the unsteady method show that the oscillation cycles for the thrust and torque are consistent, with both being ¼ the rotational cycle of the propeller blade. In addition, the thrust and torque generated by the DRPPP are approximately double that generated by the DPP. It is also seen that the presence of the pod causes a reduction in the overall thrust of the propulsor, indicating that the pod has a certain amount of resistance effect. As such, the fairing of lines in the pod design is critical to improving the overall thrust of podded propulsors.

4.2.3. Analysis of lateral force coefficients of propulsors

As was done in computing thrust, the lateral force is made dimensionless and $K_T^Z = \dfrac{T^Z}{\rho n^2 d^4}$ is set as the lateral force coefficient, where T^Z is the overall lateral force of the propulsor, and ρ, n, and d are as previously defined. This formulation gives the graphs shown in Fig. 11–12.

The unsteady computational curves for the DPP and DRPPP for advance coefficient $J = 0.7$ are shown in Fig. 11. For the two types of podded propulsors, the oscillation cycles of both the thrust and the lateral force are consistent. Furthermore, unlike the DPP, it is seen that interactions between the front and the rear propellers of the DRPPP at $J = 0.7$ not only causes changes to the value of the time-average lateral force but also significantly increases the amplitude of oscillation. although in a direction opposite to that of the DPP.

Whereas time-average values were adopted for the results of the unsteady method, the convergent solution for the computational results shown in Fig. 12 was taken directly using the steady method. Even for the same type of podded propulsor, it was found that the lateral force values derived using the steady method are very different from the time-average lateral force curve derived using the unsteady method. For the DPP, lateral force derived using both methods initial falls to zero before increasing in the reverse direction (i.e., becoming increasingly negative). Near $J = 0.7$, the respective directions of lateral force become opposite; except in this region, the absolute values of the unsteady method time-average lateral force are consistently smaller than those of the steady method. For the DRPPP, computational results for the lateral force using the steady method similarly exhibit a trend of initial reduction followed by an increase in the reverse direction. However, there is no change in the direction of the lateral force under the unsteady method; furthermore, under this method the magnitude of variation in lateral force is small for $J = 0.6$–0.8.

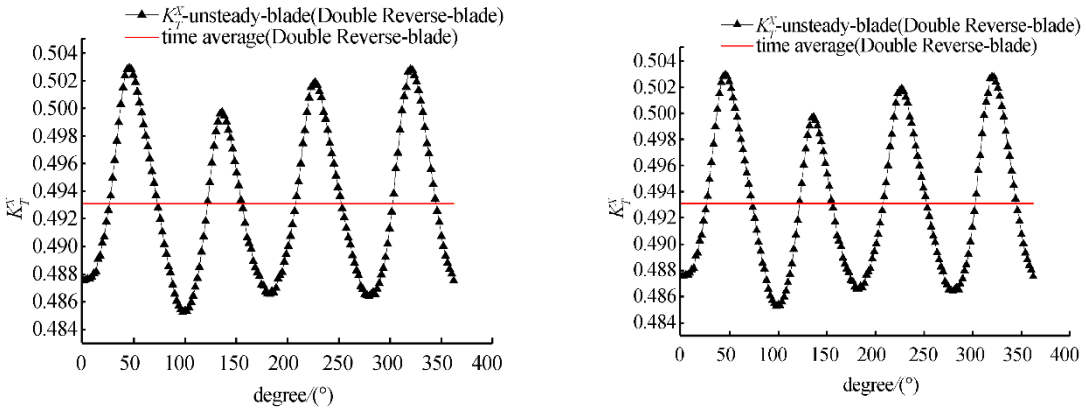

(a) DPP (b) DRPPP

Fig. 8 Comparing DPP and DRPPP: Thrust coefficient of propeller blade (J = 0.7)

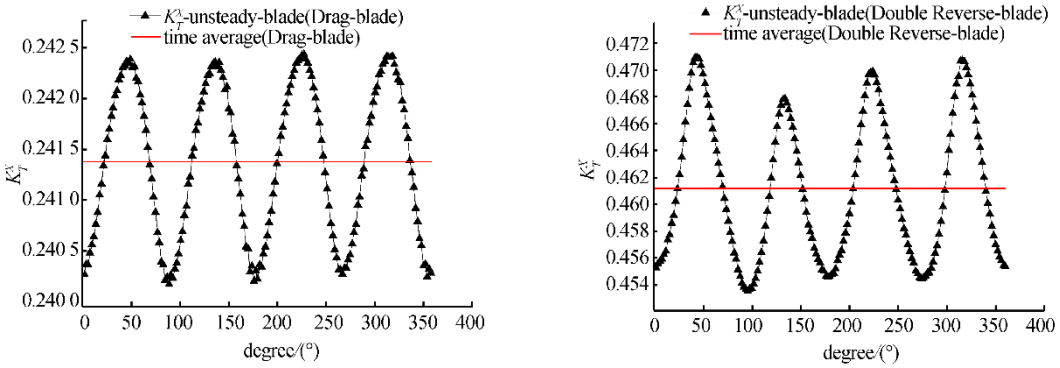

(a) DPP (b) DRPPP

Fig. 9 Comparing DPP and DRPPP: Overall thrust coefficient (J = 0.7)

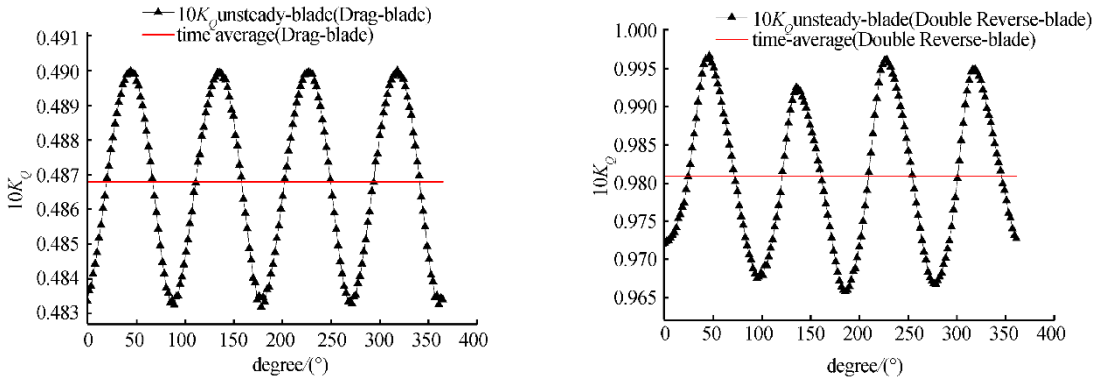

(a) DPP (b) DRPPP

Fig. 10 Comparing DPP and DRPPP: Torque coefficient (J = 0.7)

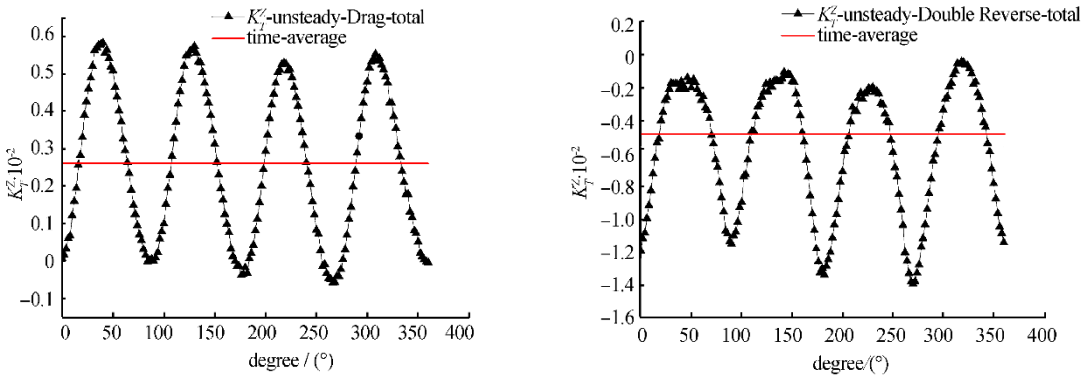

(a) DPP (b) DRPPP

Fig. 11 Comparing DPP and DRPPP: Overall lateral force coefficient (J = 0.7)

4.2.4. Force comparison for various components of podded propulsors

(a) Strut (unsteady)

The unsteady curves for the *X*-directional force and lateral force coefficients of the strut of both types of podded propulsors at J = 0.7 are shown in Figs. 13 and 14, respectively. During one rotational cycle of the propeller, the *X*-directional force of both types of podded propulsors oscillates four times, as does the lateral force of the DPP. However, the lateral force of the DRPPP oscillates eight times per cycle, indicating that the interaction of the front and rear propellers results in a doubling of the oscillation frequency. However, Fig. 11(b) shows that the lateral force of the strut has no impact on the oscillation cycle of the overall lateral force. This confirms that, at an advance coefficient of 0.7, the percentage composition of strut lateral force is minimal.

The time-average values of the lateral force and *X*-directional force coefficients for the strut are larger for the DRPPP than for the DPP; this indicates that the resistance caused by the strut is greater for the DRPPP than for the DPP. Instability also increases with the amplitude of oscillation of the lateral force. From a directional perspective, the *X*-directional forces exerted on the pods of both types of podded propulsors are similar but the directions of the lateral forces are opposite.

(b) Pod (unsteady)

The unsteady curves for the *X*-directional force and lateral force coefficients of the pods of both types of podded propulsors at J = 0.7 are shown in Figs. 15 and 16, respectively. As the pod is the main component of a podded propulsor, it is essential to analyze the force exerted on it. Based on the *X*-directional force and lateral force coefficient curves of the pod, it can be seen that at J = 0.7 the dynamics differ for the pod and strut. Specifically, for both types of podded propulsors, the oscillation frequency of the pod under lateral forces in two directions is consistent. Furthermore, the time-average *X*-directional force of the DPP pod is significantly larger than that of the DRPPP pod. This shows that the DRPPP has improved pod resistance performance and reduced resistance.

In terms of lateral force, at J = 0.7 the time-average values simulated for both types of podded propulsors are similar. However, the DRPPP's amplitude is significantly larger than that of the DPP, and peak and valley values have opposite signs. This indicates that the oscillation caused by lateral force is more intense for the DRPPP and is coupled with changes in the direction of oscillation. Nevertheless, the time-average value is negative.

(c) Proportion of lateral force on various components

After computing the time-average lateral force produced by the four components of the podded propulsor (propeller blade, pod, strut, and propeller hub) using the unsteady and steady methods, the absolute values were obtained and summed up. Then, the percentage composition of lateral force by component was calculated under various advance coefficients and the respective curves were plotted (Figs. 17 and 18).

For the DPP, the percentages accounting for the strut and propeller blade are relatively high. The unsteady time-average curve indicates that the percentage composition of the propeller blade, pod, and hub all increase initially before decreasing, whereas that of the strut does the opposite. In addition, below J = 0.7 the proportion of lateral force from the strut is consistently the highest, after which the strut and propeller blade alternate as the highest producing component. In the steady time-average curve, the lateral force of the strut remains predominant throughout.

The unsteady time-average curve for the DRPPP indicates a larger difference in the percentage composition of the lateral force from the strut, with a minimum inflection point occurring at J = 0.6. The lateral force of the pod accounts for only a very small proportion throughout, in contrast to the steady time-average curve, where the lateral force of the strut exhibits overall increase while changes for the other components are relatively minor.

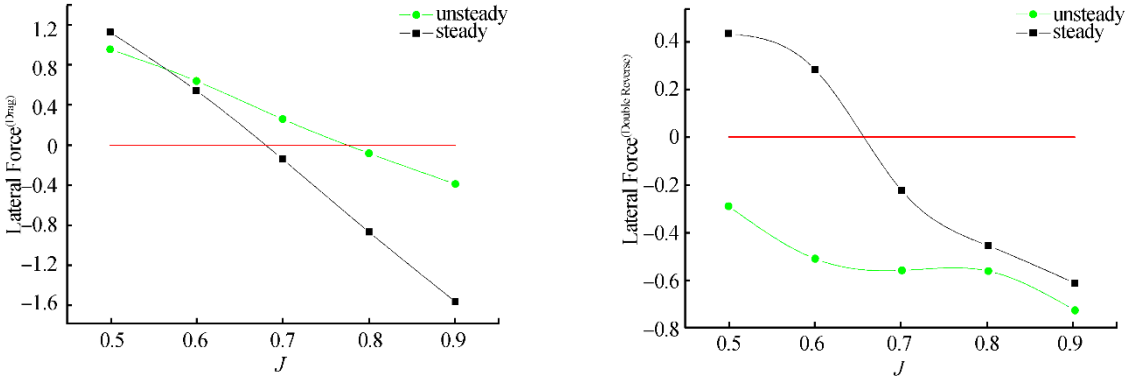

(a) DPP (b) DRPPP

Fig. 12 Comparing DPP and DRPPP: Overall time-average lateral force coefficient under various advance coefficients

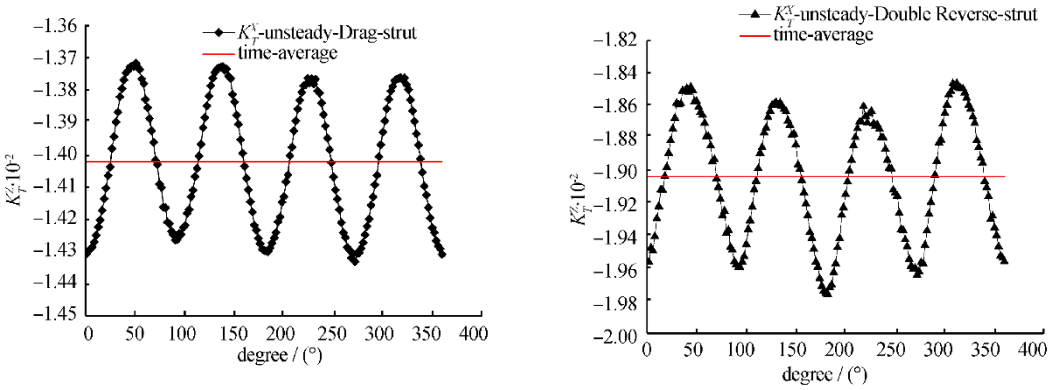

(a)DPP (b)DRPPP

Fig. 13 Comparing DPP and DRPPP: *X*-directional force coefficient of strut (J = 0.7)

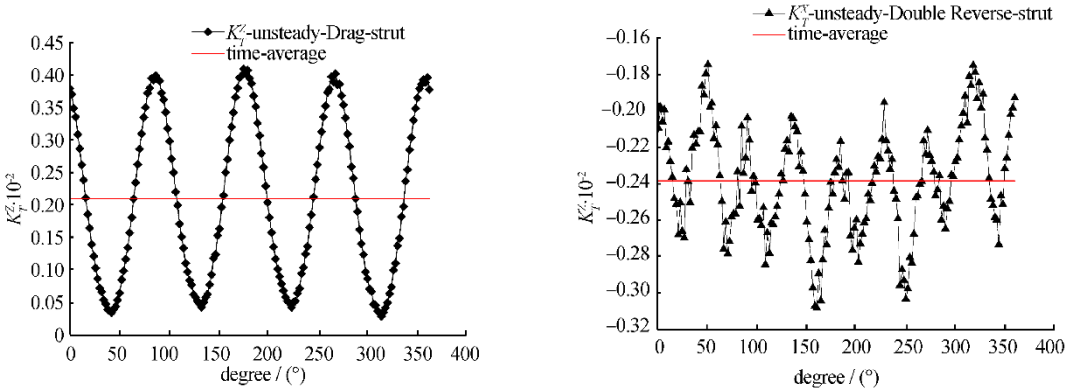

(a)DPP (b) DRPPP

Fig. 14 Comparing DPP and DRPPP: Lateral force coefficient of strut (J = 0.7)

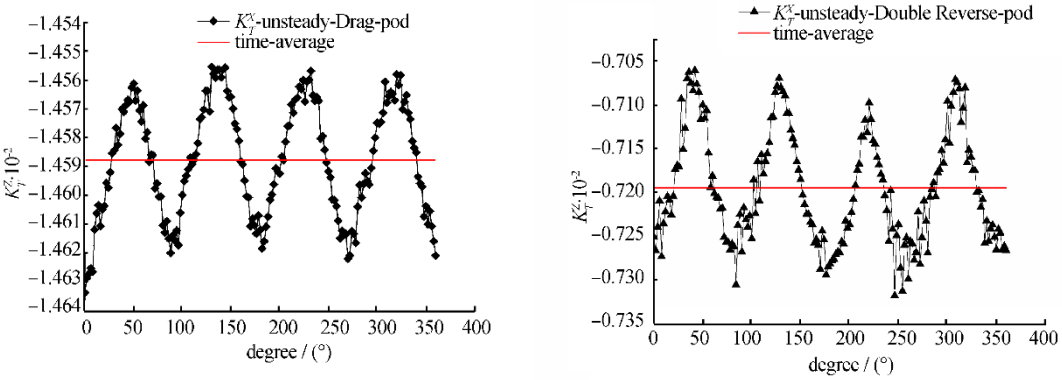

(a) DPP (b) DRPPP

Fig. 15 Comparing DPP and DRPPP: *X*-directional force coefficient of pod (J = 0.7)

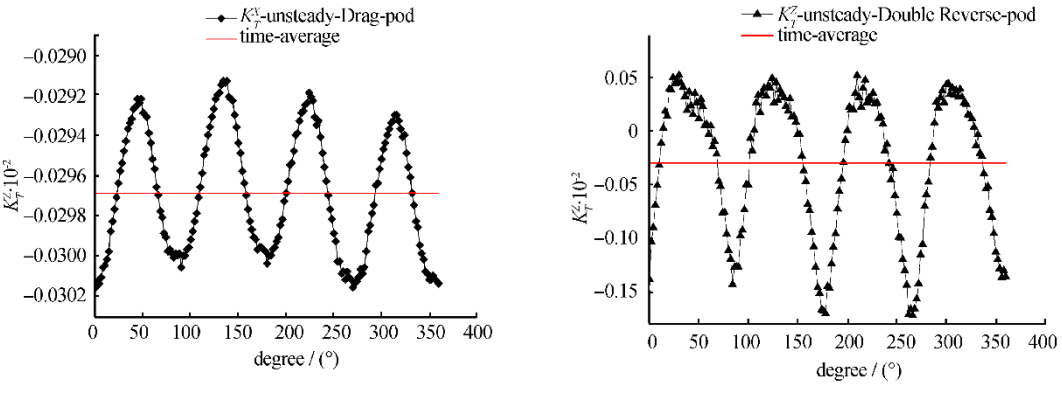

(a) DPP (b) DRPPP

Fig. 16 Comparing DPP and DRPPP: Lateral force coefficient of pod (J = 0.7)

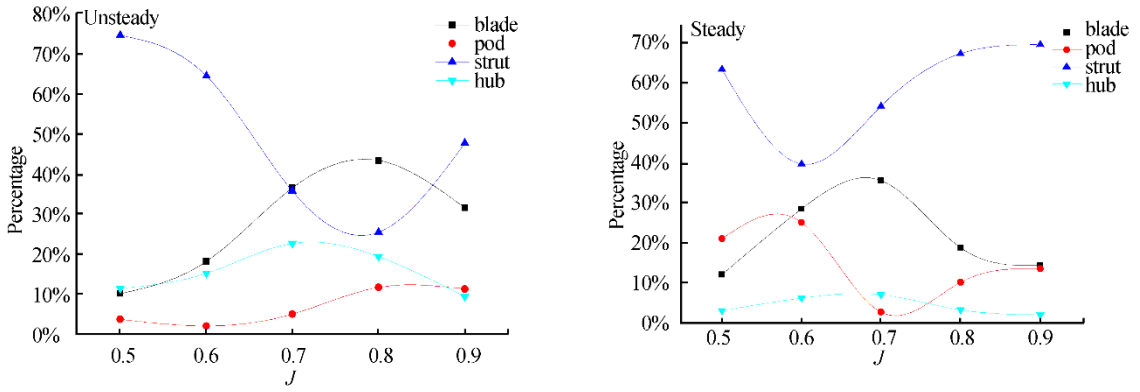

(a) Unsteady time-average (b) Steady time-average

Fig. 17 DPP: Change in percentage composition of time-average lateral force with variations in advance coefficient

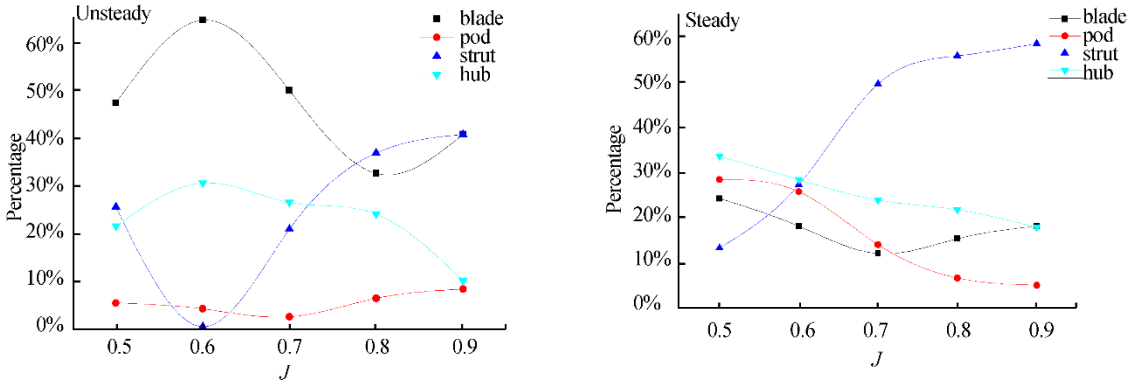

(a) Unsteady time-average (b) Steady time-average

Fig. 18 DRPPP: Change in percentage composition of time-average lateral force with variations in advance coefficient

4.3 Comparative analysis of velocity and force clouds

4.3.1 Velocity and force clouds of DPP

Fig. 20 shows the velocity clouds of various sectional positions of the DPP at J = 0.7. The various sectional positions and force distributions obtained under the unsteady method are shown in Fig. 20.

Comparing the steady and unsteady computational results, it is seen from the velocity clouds that, under both methods, the axial velocity distribution gradually increases from the pod outwards and then gradually decreases. The peak velocity values occur in the propeller blade area. However, there is significantly more continuity and symmetry in velocity distribution under the unsteady method.

The force clouds show that the force distribution on the pod is relatively even. A peak force appears where the pod and the front edge of the strut are in contact. To avoid such situations in engineering practices, the fairing of lines must be made as smooth as possible. The rotation of the propeller causes the rotation of the streamline in-wake field to be right-handed; correspondingly, in Fig. 20 high pressure is seen at the right-front part of the strut and a pressure low is seen at the end part.

4.3.2 Velocity and force clouds of DRPPP

The velocity clouds of various sectional positions of the DRPPP are shown in Figs. 21 and 22. The positions of these are the same as for the DPP: (i) between the front propeller blade and the pod; (ii) at the central portion of the strut; and (iii) between the rear propeller blade and the pod. A comparison of the steady and unsteady computational results for the DRPPP at J = 0.7 shows that they are similar to those for the DPP. Specifically, the velocity distribution under the unsteady method is more continuous. The velocity distribution at the middle portion of the pod is also more uniform. These findings are more consistent with reality than the DPP findings.

At the same time, it is by comparing the force clouds in Figs. 20 and 21 that the force exerted on the rear edge of the strut of the DRPPP is lower than that exerted on the corresponding position of the DPP. This indicates that there is a corresponding increase in the force differential between the front and the rear of the DRPPP. This is an important factor that accounts for the greater resistance generated by the strut of the DRPPP.

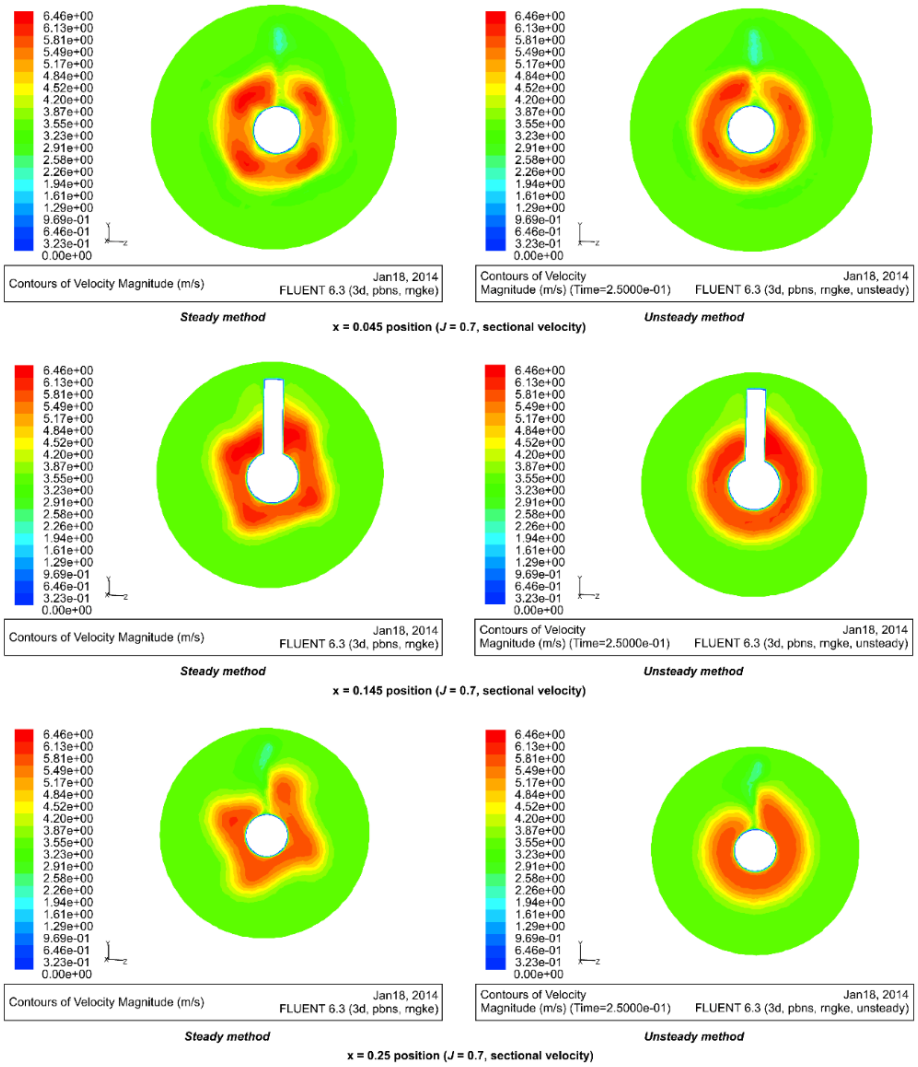

Fig. 19 DPP: Velocity clouds of various sectional positions

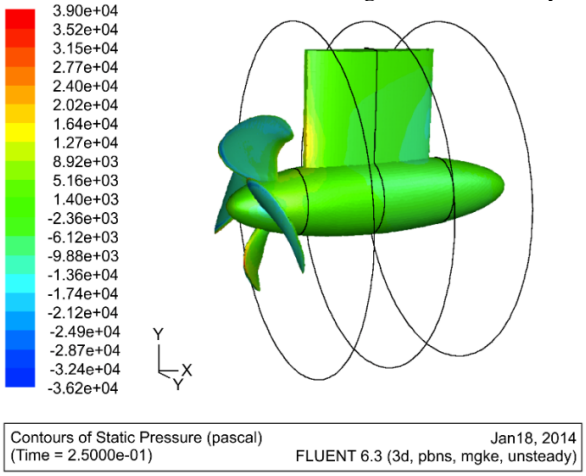

Fig. 20 DPP: Schematic diagram of three positions (X = 0.045, 0.145, and 0.25 m) and force distribution under unsteady method

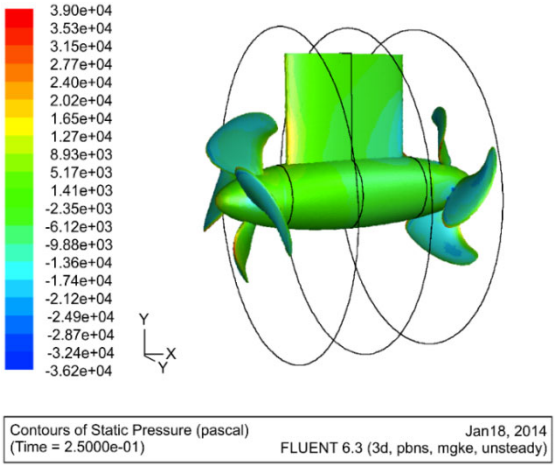

Fig. 21 DRPPP: Schematic diagram of three positions (X=0.045, 0.145, and 0.25 m) and force distribution under unsteady method

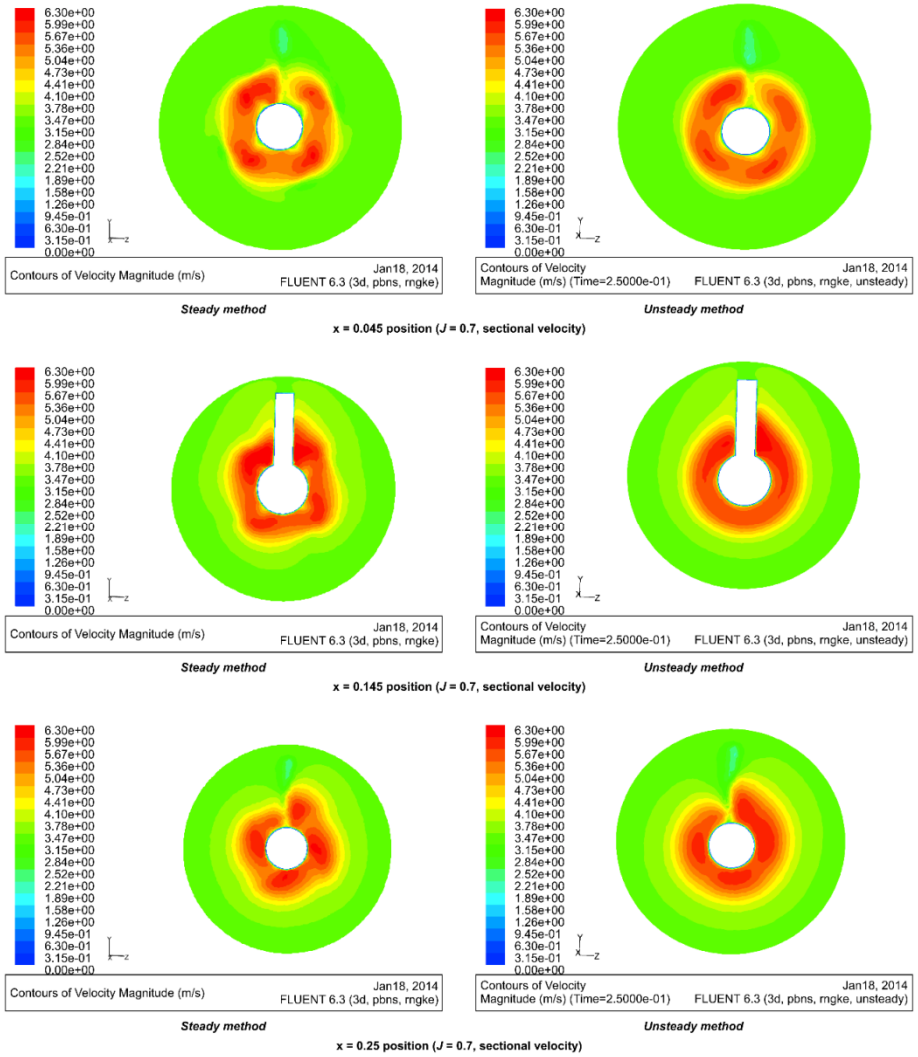

Fig. 22 DRPPP: Velocity clouds of various sectional positions

5 Conclusion

The following preliminary conclusions were derived from the analysis of the computational results.

The thrust and torque of the DPP computed using the steady and unsteady methods were closer to the corresponding experimental values. The error margin for both was within 5%, indicating that the two forecasting methods are relatively reliable. The unsteady method had a slightly higher degree of accuracy, but it imposed greater demands on the computing system. The simulation results for the thrust and torque of the DRPPP were relatively close, with a difference of less than 2%. Currently, there is no corresponding experimental data for comparison purposes.

Overall, the lateral force of the DPP derived using the steady method was generally similar to the time-average value simulated using the unsteady method. The overall lateral force reduced initially before increasing in the opposite direction. The distinction between the methods lies in when this reversal occurred in simulation: for the steady method, it was in the vicinity of J = 0.7, while for the unsteady method it was near J = 0.8.

For the DRPPP, there was a greater difference between the computational results of the two methods. Under the steady method, changes in the simulation results occurred in the vicinity of J = 0.7. However, the direction of the time-average lateral force under the unsteady method remained unchanged but reduced continuously in the reverse direction, essentially tending toward a flat line when J = 0.6–0.8. At J = 0.7, interactions between the front and rear propellers, which rotate in reverse directions, caused the behavior of the time-average lateral force relative to differ from that of the DPP. Furthermore, the amplitude of oscillation increased significantly and reversed direction relative to the oscillation of the DPP.

In terms of percentage composition of lateral force, the strut and propeller blade of the DPP had a larger proportion than the pod and propeller hub. Under the unsteady method, the oscillation cycle of the lateral force of the various components was ¼ that of the propeller's rotational cycle. The computational results of the two methods for the DRPPP varied greatly. The unsteady results indicate that the lateral force of the propeller blade formed the largest

proportion throughout. At J = 0.6, a sudden inflection point appeared in the downward-trend of the lateral force of the strut, after which the value gradually increased. At J = 0.7, the oscillation frequency of the strut was double that of the other components; however, this did not affect the oscillation cycle of the overall lateral force because the strut accounted for only ~20% of the total figure. The computational results produced under the steady method indicate that the proportion of lateral force produced by the pod grew in a continuous manner as the advance coefficient increased. By contrast, the pod and propeller hub exhibited a downward trend. There was a slight increase in lateral force by the propeller blade above J=0.7, although its proportional contribution remained small.

Velocity clouds for various sectional positions of the podded propulsors were computed using the two methods. The results indicate that, for both the DPP and DRPPP, the continuity of the flow field was poorer under the steady method. On the other hand, the velocity field distribution for both types was more reasonable under the unsteady method and theoretically more convincing. Also, for both propulsor types the rotational direction of the front propeller influenced the pressure distribution downstream over the pod and strut. Based on these results, this study concludes that the unsteady method is more accurate for forecasting the hydrodynamic performance of podded propulsors.

References

Bal S, Güner M, 2009. Performance analysis of podded propulsors. *Ocean Engineering*, **36**(8), 556-563.
DOI: 10.1016/j.oceaneng.2009.05.012

Cao ML, Wang GL, Zhu M, 2003. Experimental research on the hydrodynamic performance of podded propulsors. *Journal of Shanghai Jiaotong University*, **8**, 1198-1200.
DOI：10.3321/j.issn:1006-2467.2003.08.014

Guo CY, Ma N, Yang CJ, 2009a. Numerical simulation of a podded propulsor in viscous flow. *Journal of Hydrodynamics, Ser. B*, **21**(1), 71-76.
DOI: 10.1016/S1001-6058(08)60120-1

Guo CY, Yang CJ, Ma N, 2009b. CFD simulations for a drag podded propulsor operating at oblique angles. *Journal of Ship Mechanics*, **06**, 861-872.
DOI: 10.3969/j.issn.1007-7294.2009.06.003

Guo CY, Hu WT, Yang CJ, Ma N, 2010a. Research on podded propulsors with varied geometry in viscous flow. *China Ocean Engineering*, **24**(4), 693-708.

Guo CY, Yang CJ, Ma N, 2010b. Computation of steady hydrodynamic performance of podded propulsors. *Journal of Ship Mechanics*, **14**(1), 30-31.
DOI: 10.3969/j.issn.1007-7294.2010.01.004

Liu P, Islam M, Veitch B, 2009. Unsteady hydromechanics of a steering podded propeller unit. *Ocean Engineering*, **36**(12-13), 1003-1014.
DOI: 10.1016/j.oceaneng.2009.05.012

Li W, Wang L, Yang CJ, Yang C, 2009. Steady hydrodynamic performance of podded propulsors. *Journal of Shanghai Jiaotong University*, **43**(2), 204-207.

Ma C, 2006. *Research on the hydrodynamic performance of POD propulsors*. PhD thesis, Harbin Engineering University, Harbin, China.

Mewis F, 2001. The efficiency of podded propulsion. *Proceedings of HADMAR 2001*, Varna, Bulgaria, 47-48.

Ohashi K, Hino T, 2003. Flow calculation of a ship with a podded propulsor. *Proceedings of the 6th Numerical Towing Tank Symposium*, Rome, Italy, 15-24.

Shamsi R, Ghassemi H, 2014. Hydrodynamic analysis of puller and pusher of azimuthing podded drive at various yaw angles. *Proceedings of the Institution of Mechanical Engineers Part M–Journal of Engineering For The Maritime Environment*, **228**(1), 55-69.

The Propulsion Committee, 2002. The Propulsion Committee of 22nd ITTC. Final report and recommendations to the 23rd ITTC. *Proceedings of 23rd ITTC*. Hamburg, Germany, 2002, 97-98.

Wang C, Huang S, Chang X, Guo CY, 2011. Impact of propeller-rudder interactions on performance: A study based on moving mesh and the RNG k-ε turbulence model. *Journal of Ship Mechanics*, **7**, 715-721.

Yang CJ, Qian ZF, Ma C, 2003. Impact of the POD on the hydrodynamic performance of propellers. *Journal of Shanghai Jiaotong University*, **8**, 1229-1233.
DOI: 10.3321/j.issn:1006-2467.2003.08.022

Zhang W, 2008. *Simulation and analysis of hydrodynamic performance of podded propulsors*. Master thesis, Shanghai Jiaotong University, Shanghai, 55-57.

Zhuang GY, Cai HP, Ma C, Qian ZF, Chen K, Yin BR, 2013. Research on the CFD modeling method to forecast the hydrodynamic performance of double-propeller podded propulsors. *Proceedings of the 25th National Conference on Hydrodynamics and 12th National Congress on Hydrodynamics*, Zhoushan, China, 947-954.